

See discussions, stats, and author profiles for this publication at: <https://www.researchgate.net/publication/23936650>

Molecular Dynamics Simulation of the Low-Temperature Partial Oxidation of CH₄

ARTICLE *in* THE JOURNAL OF PHYSICAL CHEMISTRY A · FEBRUARY 2009

Impact Factor: 2.69 · DOI: 10.1021/jp809576k · Source: PubMed

CITATIONS

12

READS

34

2 AUTHORS, INCLUDING:



Alister J Page

University of Newcastle

57 PUBLICATIONS 650 CITATIONS

SEE PROFILE

Molecular Dynamics Simulation of the Low-Temperature Partial Oxidation of CH₄

Alister J. Page* and Behdad Moghtaderi

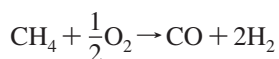
*Priority Research Centre for Energy, Discipline of Chemical Engineering, Faculty of Engineering and Built Environment, The University of Newcastle, University Drive, Callaghan, NSW 2308, Australia**Received: October 29, 2008; Revised Manuscript Received: December 10, 2008*

Low-temperature partial oxidation of methane was investigated using reactive molecular dynamics (MD) and quantum mechanical (QM) methods. In particular, the ReaxFF hydrocarbon force field [Chenoweth, K.; et al. *J. Phys. Chem. A* 2008, 112, 1040] was employed to simulate a [20 CH₄ + 10 O₂] model system at 500 °C. The chemical mechanism of the partial oxidation of methane was proposed on the basis of analysis of the computed trajectory of this model system. The partial oxidation of methane was observed to be initiated by the abstraction of hydrogen from CH₄ by O₂ and the atomization of CH₄ itself. Subsequent radical recombination between hydrogen atoms and the dehydrogenation of CH₄ were the primary pathways by which H₂ was formed. In agreement with current models of low-temperature combustion, radicals including H₃C–OO and H₂C–OO were also observed during the MD simulation. The observed reaction mechanism was subsequently analyzed using QM methods. For instance, structural features of prominent radical species observed during the MD simulation were analyzed using density functional theory (DFT) and coupled-cluster (CCSD(T)) methods. Enthalpies of reaction of all observed chemical processes were calculated using DFT and the W1 composite method. Where possible, comparisons with experimental data were made.

Introduction

Hydrogen is thought to be a crucial component of sustainable energy scenarios in the future.¹ There are several reasons why this is the case. Most importantly, hydrogen is a clean fuel (oxidation yields water as the only chemical product) and exhibits a relatively large energy density (ca. 120–140 MJ kg^{−1}). The consumption of hydrogen in the production of heat/power is also ideally suited to fuel cell technology. Despite these desirable qualities, pure hydrogen does not occur naturally on earth.² The success of using hydrogen in the context of sustainable energy production therefore depends entirely on its safe and efficient manufacture from other, primary fuel sources.

Myriad alternatives for the generation of hydrogen have been proposed to date.^{3–7} Increasingly, however, the generation of hydrogen from the partial oxidation of methane (POM) has been considered to be an attractive option. This reaction,



although only slightly exothermic ($\Delta_r H^\circ(298.15 \text{ K}) = -36 \text{ kJ mol}^{-1}$),⁸ is extremely fast, particularly at high temperatures.⁹ In addition, methane is readily available in many parts of the world. This chemical process is also adaptable to microscale fuel cells, making it suitable for mobile/onboard applications.¹⁰ For example, our group^{11,12} recently implemented hydrogen generation via POM in a microscale reactor.

There are a number of reviews available concerning various aspects of both noncatalytic and catalytic POM.^{8,13–15} Most recently, Enger et al.⁹ reviewed the reaction mechanisms associated with transition-metal-catalyzed POM. The first investigations of catalytic POM were performed by Liander,¹⁶ Padovani and Franchetti,¹⁷ and Prettre et al.¹⁸ These investigations demonstrated that higher temperatures (i.e., greater than

850 °C) promote both methane conversion and CO/H₂ selectivity. Noncatalytic POM at temperatures greater than ca. 1000 °C is now a commercially viable technology.¹³ York et al.⁸ reported that high pressure impedes both methane conversion and product selectivity. These dependencies on both temperature and pressure of noncatalytic and catalytic POM were also recently reproduced on the microscale.¹² Despite the extent of the literature concerning the reaction mechanisms and kinetics of POM, no investigation has reported atomistic information regarding the initial or fundamental chemical events responsible for the conversion of methane at 500 °C. Such low temperature systems are particularly attractive from an energy efficiency perspective. However, several quantum mechanical (QM) investigations of catalytic POM reaction mechanisms have been reported (see ref 9 and references therein). To the best of our knowledge, no reported investigations have addressed the fundamental chemical processes of the POM using atomistic molecular dynamics (MD).

Although correlated QM methods increasingly provide reliable structural, thermochemical, and kinetic data for many atomic and molecular species, their computational expense limits their practical application to only the simplest reactive systems. Conversely, traditional MD force fields allow for the simulation of large-scale properties (i.e., in excess of millions of atoms) and are applicable to a wide range of species. Nevertheless, MD methods generally fail to describe the processes of bond breaking and bond formation. The force field of Brenner¹⁹ developed for hydrocarbons is an exception, in that it allows chemical bonds to be broken. The approach of Brenner is an extension of the bond order/bond distance relationship introduced by Tersoff.²⁰ In this case, the connectivity of every atom in the system of interest is determined at each iteration and is a function of bond order. This allows the connectivity of the system to vary with time. However, the Brenner force field lacks an explicit description of Coulombic and van der Waals interactions. Dissociative potential energy surfaces predicted

* To whom correspondence should be addressed. E-mail: alister.page@newcastle.edu.au.

using the Brenner force field are therefore often lacking in a quantitative sense. Similar “reactive” force fields include the bond energy bond order method of Johnston and co-workers^{21,22} and the VALBOND method of Landis and co-workers.^{23–25} The former of these force fields is based on the relationship between bond order and bond length proposed by Pauling.²⁶

A more recent approach is that of van Duin and co-workers, who investigated hydrocarbons,^{27,28} nitramines,²⁹ oxides of various main group metals,^{30,31} carbon–silicon polymers,³² and transition-metal catalysis^{33–35} using their ReaxFF force field. This force field explicitly includes descriptions of Coulombic and van der Waals interactions and also describes the valence/torsion angles, bond conjugation, and polarization effects at each iteration of the MD simulation. These structural phenomena are therefore included in the description of bond formation and bond breaking. At small internuclear distances, the repulsive force experienced between atoms is controlled by shielding functions. The parameters defining the ReaxFF force field are tuned against an extensive set of structural and energetic data that were calculated using density functional theory (DFT). Chenoweth et al.²⁸ recently extended the ReaxFF hydrocarbon force field QM training set to include chemical reactivity and transition-state data typically observed during hydrocarbon oxidation. Hence, a more complete chemical description of low-temperature POM would be attained using this method.

We wish to present here a theoretical investigation of low-temperature POM. The ReaxFF hydrocarbon force field reported by van Duin et al.^{27,28} will be used to simulate the reaction between CH₄ and O₂ at 500 °C. The low-temperature POM was modeled using a model system of CH₄ and O₂ molecules in the stoichiometric ratio 2:1. The mechanism observed from analysis of the computed trajectory of the system will subsequently be discussed. Structural and energetic features of this mechanism will then be analyzed in greater detail. First, the equilibrium structures of prominent radical species observed during the simulation will be investigated using QM methods. Enthalpies of several reactions observed in the MD simulation will then be reported using QM methods. It is hoped that the analysis presented in this work will furnish a more complete atomistic understanding of the fundamental processes observed in low-temperature oxidative processes of simple hydrocarbons.

Computational Methods

Molecular Dynamics Simulations. A periodic system of 20 CH₄ and 10 O₂ molecules was simulated using the ReaxFF force field.^{27,28} The dimensions and density of the system were 20 × 15 × 15 Å³ and 0.40 kg dm⁻³, respectively. Throughout the MD simulation, the number of atoms and the volume/temperature of the periodic system were held constant (conditions denoted by NVT). The system temperature was maintained via a Berendsen thermostat³⁶ with a 2.5-fs damping constant. The system was initially equilibrated at 500 °C (773.15 K) for 100 ps using NVT-MD with a 0.1-fs time step. Chenoweth et al.²⁸ employed this time step for high-temperature (2500 K) MD hydrocarbon oxidation and noted that this time step allows for a consistent description of the charges and bond orders in the system (both of which can change at each time step), and therefore facilitated a consistent description of chemical processes. An NVT-MD time step of 0.1 fs is anticipated to suffice in this work. Fluctuations in the kinetic energy and dynamics properties of individual particles in an MD simulation are not significantly altered using damping constants ca. 1–2 orders of magnitude greater than Δt , such as that employed here. Nevertheless, fluctuations in the total energy of the system are,

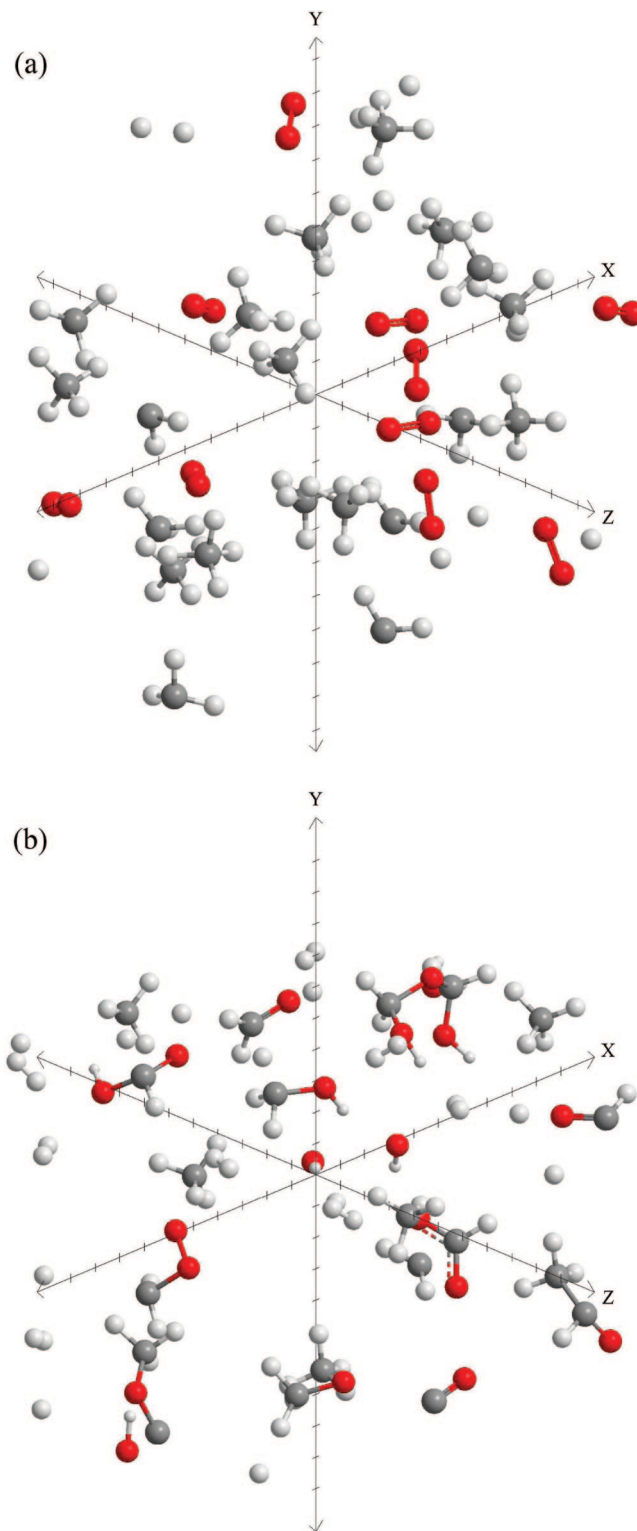


Figure 1. [20 CH₄ + 10 O₂] system after (a) 100-ps NVT-MD equilibration at 773.15 K and (b) 3000-ps NVT-MD reaction at 773.15 K.

to a large extent, artifacts of MD approaches and are associated with smaller temperature damping constants (i.e., <0.01 ps).³⁶ Reactions between O–C and O–H were prevented during the 100-ps equilibration period by eliminating the bond parameters describing these interactions from the force field. The final equilibrated system geometry is shown in Figure 1a. The equilibrated system geometry was then employed in a 500 °C (773.15 K) NVT-MD simulation that employed a simulation

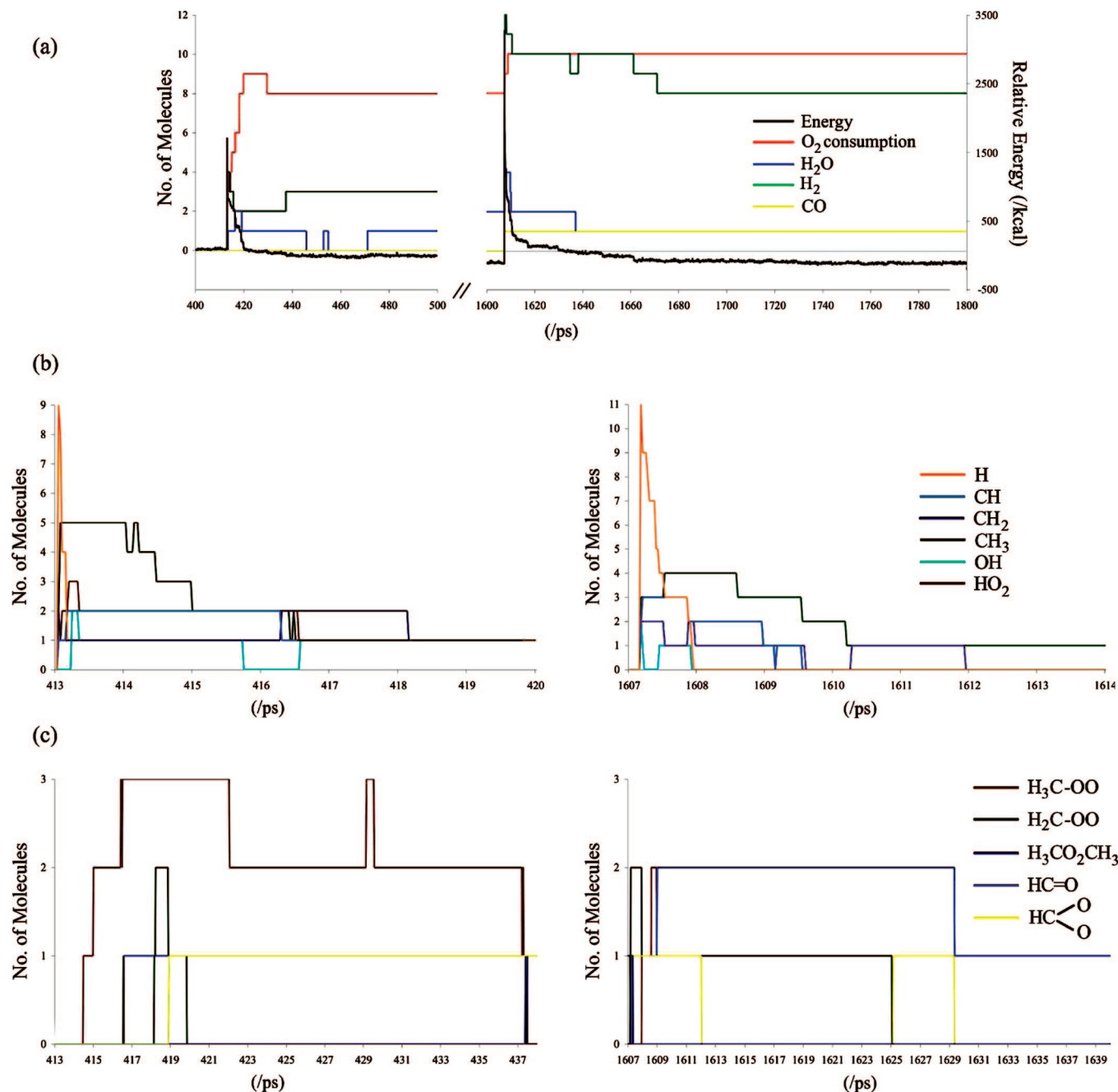


Figure 2. Molecular composition and total energy of the NVT-MD simulation as a function of time. (a) Major products. (b) Initial radical species. (c) Minor products.

time step of 0.1 fs. The latter NVT-MD simulation was continued for 3000 ps. The final system composition is shown in Figure 1b. (It is noted here that apparent molecular fragmentation of species in the vicinity of the boundaries of the periodic box (observed in Figure 1) is unavoidable.) The pressure employed throughout these NVT-MD simulations was 101.3 kPa.

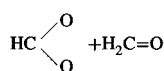
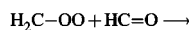
Quantum Mechanical Calculations. Equilibrium structural parameters (including bond lengths (R_e) and bond angles (θ_e)) of prominent radical species observed during the initiation of the POM were calculated using the B3LYP hybrid DFT functional^{37,38} and coupled-cluster with singles, doubles, and perturbative triples (CCSD(T)). Comparison with the latter method allows us to gauge the effects of dynamical electron correlation more accurately. The 6-311G** one-electron basis set³⁹ was used in both DFT and CCSD(T) calculations. This

basis set was also used in the development of the hydrocarbon ReaxFF force field parameters. These parameters were optimized so as to reproduce the energy corresponding to the lowest energy spin state of each molecule.²⁸ In order that consistency with the results of the ReaxFF simulation was attained, it was ensured that all DFT and CCSD(T) energies/structures corresponded to those of the lowest energy spin states. For both B3LYP/6-311G** and CCSD(T)/6-311G** methods, a spin-restricted Hartree–Fock determinant was employed as the reference function for all open-shell species. Both the B3LYP/6-311G** and CCSD(T)/6-311G** methods employed a frozen core consisting of the C and O 1s atomic orbitals.

The thermochemistry of several reactions observed during the NVT-MD simulation was also investigated quantum mechanically. Enthalpies of reaction at 298.15 K ($\Delta_r H^\circ(298.15 \text{ K})$) were calculated using the ReaxFF force field and B3LYP/

TABLE 1: Comparison of Experimental and Theoretical Reaction Enthalpies (kcal mol⁻¹) for Reactions Observed during the ReaxFF Simulation

| Reaction | $\Delta_r H^\circ(298.15 \text{ K})$ | | | |
|---|--------------------------------------|--------|--------|----------------------|
| | REAXFF | DFT | W1 | Expt. |
| $\text{CH}_4 \rightarrow \text{C} + 4\text{H}$ | 463.3 | 400.2 | 393.8 | 395.7 ¹ |
| $\text{C} + \text{H} \rightarrow \text{CH}$ | -118.7 | -81.3 | -79.9 | -81.39 ¹ |
| $\text{CH} + \text{H} \rightarrow \text{CH}_2$ | -115.3 | -101.9 | -100.2 | -101.8 ¹ |
| $\text{CH}_4 + \text{H} \rightarrow \text{H}_2 + \text{CH}_3$ | 1.4 | 2.2 | 0.6 | 0.6 ¹ |
| $\text{CH}_4 + \text{O}_2 \rightarrow \text{HO}_2 + \text{CH}_3$ | 41.2 | 57.3 | 56.3 | 53.2 ¹ |
| $\text{CH}_3 + \text{O}_2 \rightarrow \text{H}_3\text{C}-\text{OO}$ | -48.1 | -29.7 | -31.2 | -30.9 ² |
| $\text{CH}_2 + \text{O}_2 \rightarrow \text{H}_2\text{C}-\text{OO}$ | -59.4 | -71.0 | -74.0 | |
| $\text{CH} + \text{HO}_2 \rightarrow \text{HC}=\text{O} + \text{OH}$ | -118.0 | -124.2 | -126.8 | -122.8 ¹ |
| $\text{O}_2 + \text{H} \rightarrow \text{HO}_2$ | -69.8 | -48.2 | -47.6 | -51.6 ¹ |
| $\text{O}_2 + \text{C} \rightarrow \text{CO} + \text{O}$ | -150.7 | -132.7 | -138.7 | -139.8 ¹ |
| $\text{HO}_2 + \text{H} \rightarrow \text{H}_2\text{O}_2$ | -98.7 | -81.5 | -86.6 | -85.1 ¹ |
| $\text{H}_2\text{O}_2 \rightarrow 2\text{OH}$ | 45.2 | 47.5 | 50.2 | 51.17 ¹ |
| $\text{OH} + \text{H} \rightarrow \text{H}_2\text{O}$ | -114.2 | -113.4 | -118.2 | -119.22 ¹ |
| $\text{OH} + \text{H}_2 \rightarrow \text{H}_2\text{O} + \text{H}$ | -4.7 | -10.1 | -15.0 | -15.01 ¹ |
| $\text{H}_3\text{C}-\text{OO} + \text{CH}_3 \rightarrow \text{H}_3\text{C}-\text{OO}-\text{CH}_3$ | -70.7 | -60.2 | -64.5 | |



| | | |
|--------|-------|-------|
| -128.9 | -96.2 | -94.9 |
|--------|-------|-------|

¹ See ref 58. ² See ref 60.

formation of CH₄ and O₂ in the NVT-MD simulation was therefore not observed via this pathway. The formation of the methylperoxy radical was observed soon after initiation at 419.5 ps. This radical species was present at various concentrations for the remainder of the NVT-MD simulation, as is evident from Figure 2c. It has been noted in a number of investigations (see ref 45 and references therein) that at atmospheric pressure the H₃C-OO radical is the main product of the [CH₃ + O₂] reaction at temperatures lower than 1000 K. At higher temperatures, however, this reaction results in association giving [H₂C-O + OH] (1000–2000 K) and [H₃C-O + O] (>2000 K). Petersen and co-workers^{46,47} established the importance of radicals such as H₃C-OO and H₃C-O with respect to the kinetics of POM at higher temperature and pressure. The latter radical is formed from the reaction between [H₃C-OO + CH₃] at 1100 K and 10 MPa.⁴⁸ The hydrogenated form of this radical (H₃C-OOH) was not observed, although its presence has been established in higher-temperature NVT-MD simulations of methane oxidation.²⁸ Nevertheless, methanol and the methoxy radical were observed at ca. 1608 and 1607 ps, respectively. The H₃C-OO radical observed corresponds to a local minimum on the ²A'' potential energy surface.⁴⁵ The observed structure of the H₃C-OO radical will be discussed at greater length below. Reaction between the methyl and methylperoxy radicals was also observed at 437.5 ps, producing dimethyl peroxide, H₃C-OO-CH₃. This reaction was exothermic and corresponded to a $\Delta_r H^\circ(298.15 \text{ K})$ of ca. -60 kcal mol⁻¹.

The formation of H₂O₂ (from the addition of H and HO₂) was observed in the NVT-MD simulation at 416.2 ps. This addition was competitive with the formation of HO₂ itself, because of the comparable concentrations of H, O₂, and HO₂ during this period. This is consistent with the conclusion of Chenoweth et al.,²⁸ who proposed that the presence of HO₂ radicals is determined by the relative levels of H, OH, and O₂ in the system. Interestingly, this consistency occurs despite a large temperature difference (ca. 1800 K). The H₂O₂ radical species dissociated quickly, forming two hydroxyl radicals.

Water was subsequently formed via two different reactions. First, addition of H to OH at 416.4 ps resulted in the formation of H₂O. The abstraction of hydrogen from H₂ also gave H₂O according to [OH + H₂ → H₂O + H]. Both of these processes are exothermic; however, the former addition process corresponded to a $\Delta_r H^\circ(298.15 \text{ K})$ value ca. 10 times that of the latter abstraction.

Following the atomization of CH₄, the [C + H → CH] and [CH + H → CH₂] recombination reactions were observed at 416.2 and 419.3 ps, respectively. This was anticipated, given the increased concentrations of free C and H during these periods of the NVT-MD simulation. These recombination reactions were also observed at 1610.3 and 1608.3 ps. However, no further hydrogenation of the methylene radical was observed. This was attributed to the presence of the competing [H + H → H₂] radical recombination reaction. The latter process was observed to be the primary mechanism by which H₂ was formed during the NVT-MD simulation and was initially observed at 416.1 ps. From Figure 2, it is evident that the sharp decrease in H concentration at 413–414 and 1607–1608 ps is accompanied by increasing concentrations of H₂, CH, and CH₂. The methyldyne radical was relatively short-lived and was not observed in the simulation after 1609 ps. The majority of H₂ present at the end of the NVT-MD simulation was formed within the first 4 ps of both reaction initiations, as observed in Figure 2a. However, H₂ formation was observed as late as ca. 437 and 2171 ps. A second, less prominent process resulting in the formation of H₂ was also observed, viz. the abstraction of H by CH₄, resulting in CH₃. This process was observed immediately after initiation at 416.1 ps and is slightly endothermic ($\Delta_r H^\circ(298.15 \text{ K}) \approx 0.6 \text{ kcal mol}^{-1}$; see Table 1).

The methyldyne and hydroperoxyl radicals also reacted, yielding the formyl (HC=O) and hydroxyl radicals. This process, observed at 420.0 ps, corresponded to a $\Delta_r H^\circ(298.15 \text{ K})$ value of ca. -123 kcal mol⁻¹. Similarly, the methylene radical combined with O₂, giving the Criegee intermediate radical, H₂C-OO. This diradical has been ascribed fundamental roles in processes such as combustion and atmospheric photochemical processes.^{49,50} Nevertheless, it was only observed for the first time very recently in mass-spectral experiments.⁴⁹ It has also been the subject of a number of ab initio investigations (see refs 51 and 52 and references therein), and debate over the electronic structure of this species is ongoing. In agreement with available theoretical data,^{51,52} the [CH₂ + O₂] reaction observed in the NVT-MD simulation of the present work was exothermic and corresponded to a $\Delta_r H^\circ(298.15 \text{ K})$ of ca. -60 kcal mol⁻¹. The H₂C-OO structure observed here corresponds to a stable intermediate structure on the ¹A' potential energy surface. According to the ab initio data of both Chen et al.⁵¹ and Fang and Fu,⁵² this diradical ultimately dissociates, producing CO, CO₂, and H₂. The reaction paths proposed by Alvarez and Moore⁵³ also yield CO, H₂O, CO₂, and H₂ from the decomposition of a formic acid intermediate. No dissociation processes of this type were observed in the present work, since reaction between the HC=O and H₂C-OO radicals occurred ca. 0.5 ps following the formation of the latter species. This reaction resulted in a planar HCO₂ radical (Figure 3) and formaldehyde. The former of these species has been investigated previously using DFT in the context of the [CH + O₂] reaction.⁵⁴ The planar HCO₂ radical observed has been identified as the ²A₁ stable intermediate structure investigated by Huang et al.⁵⁴ According to their B3LYP/6-311++G(d,p) potential energy surface, the HCO₂ radical dissociates, giving [CO₂ + H] and [CO + OH]. These respective exothermic and endothermic processes were

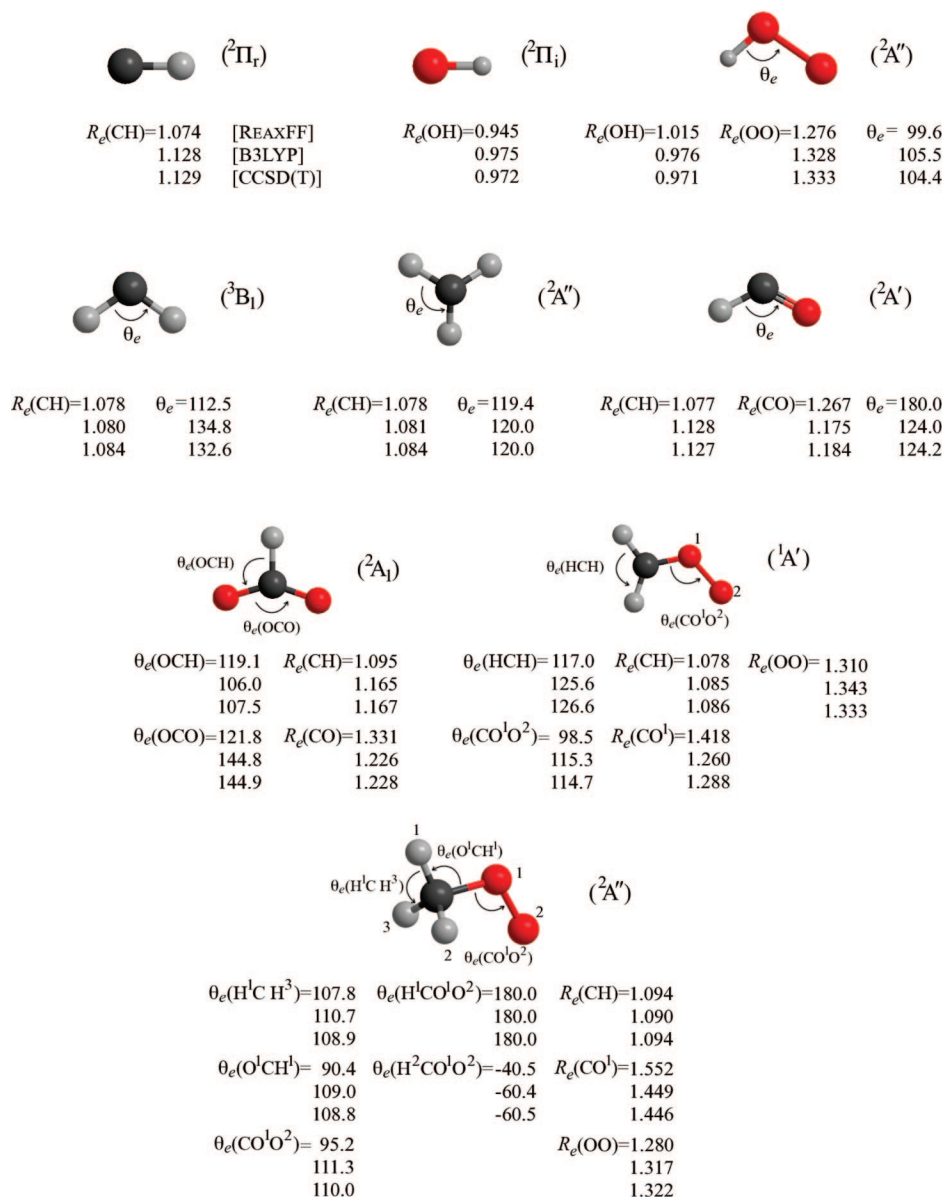


Figure 3. Comparison of the equilibrium structures of prominent radical species observed during the ReaxFF simulation, using ReaxFF, B3LYP/6-311G**, and CCSD(T)/6-311G**.

not observed in the present work. However, it is anticipated that the production of CO₂, H, CO, and OH from the decomposition of HCO₂ would be observed on longer time scales than that employed here. Nevertheless, the production of CO via [C + O₂ → CO + O] was observed at 1607.3 ps. This process exhibits a $\Delta_r H^\circ(298.15 \text{ K})$ value of ca. -140 kcal mol⁻¹, as is evident from Table 1.

Five CH₄ molecules remained in the NVT-MD simulation following 1800 ps of simulation time. This represents a 75% conversion of CH₄. After 1800 ps, all O₂ molecules present at the beginning of the simulation had been consumed. Further oxidation involving O₂ was therefore impossible. At a temperature of 500 °C, a pressure of 101.3 kPa, and a Reynolds number of 100, the total conversion of CH₄ determined in microreactor experiments was 16 ± 4%.¹² Thus, the conversion of CH₄ predicted in this work is significantly larger than that derived from experimental data. This comparison is less than ideal, however, since the extent of the simulated POM is expected to decrease at larger (i.e., micro) scales. Similarly, a comparison between QM/experimental kinetics and that derived from this

NVT-MD simulation is limited because of the “ideal” nature of the model system employed. For instance, current data⁴⁴ indicate that at 500 °C the [CH₄ + O₂ → CH₃ + HO₂] abstraction reaction possesses a rate coefficient of ca. 6.73 × 10⁻²⁶ cm³ molecule⁻¹ s⁻¹. From this rate coefficient, it is inferred that the entire POM process would occur on time scales much greater than that predicted here (ca. 3000 ps). However, at larger scales the influence of fluidic characteristics (transport properties, diffusion, etc.) and the subsequent effect on chemical reactivity must be taken into account if a realistic simulation of this chemical reaction and its kinetics is to be attained.

Quantum Mechanical Analysis of the ReaxFF Mechanism.

The presence of several radical species observed in the ReaxFF simulation discussed previously (Scheme 1) necessitates further analysis of their respective equilibrium structures. It is therefore appropriate to investigate both the equilibrium structures and thermochemistry of these species using the QM methods outlined previously.

Equilibrium Structures of Radical Species. Equilibrium structures of prominent radical species ((²Π_r)CH, (²Π_i)OH,

(²A'')HO₂, (³B₁)CH₂, (²A'')CH₃, (²A')HC=O, (²A₁)HCO₂, (¹A')H₂C=OO, and (²A'')H₃C=OO were determined using B3LYP/6-311G** and CCSD(T)/6-311G** methods. In all cases, vibrational frequencies of the equilibrated structures were calculated to ensure that the structure corresponded to a local minimum on the respective potential energy surface. These structures are given in Figure 3.

The B3LYP/6-311G** and CCSD(T)/6-311G** equilibrium structures for the smaller radical species presented in Figure 3 were in very good agreement, as anticipated. For example, *R*_e(C-H) for (²Π_g)CH, (³B₁)CH₂, and (²A'')CH₃ differed by 0.001, 0.004, and 0.003 Å, respectively. The equilibrium C-H bond length of the formyl radical differed by ca. 0.001 Å using these methods. Similarly, *R*_e(O-H) for (²Π_g)OH and (²A'')HO₂ differed by at most 0.003 and 0.005 Å, respectively. With respect to bond angles, DFT and CCSD(T) *θ*_e values for (²A'')HO₂ and (³B₁)CH₂ agreed to within 1.1 and 2.2°, respectively, while *θ*_e for (²A'')CH₃ was in exact agreement. With respect to the ²A₁ state of HCO₂, B3LYP/6-311G** and CCSD(T)/6-311G** yielded *R*_e(C-H) and *R*_e(C-O) values that differed by 0.002 Å. The equilibrium OCH and OCO bond angles for this species were also consistent using these methods. Explicitly, these bond angles differed by 1.5 and 0.1°, respectively.

Equilibrium structures calculated using the ReaxFF force field were also in generally good agreement with those using CCSD(T)/6-311G**. For instance, *R*_e(C-H) values for the methylene and methyl radicals were 0.006 Å smaller than that obtained using the latter method. Similarly, *R*_e(O-H) for (²Π_g)OH and (²A'')HO₂ differed from the CCSD(T)/6-311G** values by -0.027 and 0.044 Å, respectively. The *θ*_e values of (²A'')HO₂, (³B₁)CH₂, and (²A'')CH₃ calculated using ReaxFF differed from the CCSD(T)/6-311G** values by -4.8, -20.1, and 0.6°, respectively.

The structure of the Criegee intermediate radical (H₂C=OO) observed in the NVT-MD simulation was also investigated using B3LYP/6-311G** and CCSD(T)/6-311G**. This structure corresponds to a local minimum on the ¹A' potential energy surface.^{51,52} From Figure 3, it is evident that DFT and CCSD(T) yielded consistent structural data. For example, B3LYP/6-311G** and CCSD(T)/6-311G** *R*_e(C-H), *R*_e(C-O), and *R*_e(O-O) values differed by 0.001, 0.028, and 0.010 Å, respectively. In addition, *θ*_e(HCH) and *θ*_e(CO¹O²) values calculated using these methods agreed to within 1.0 and 0.6°, respectively. These data were also consistent with the complete active space (CASSCF) calculations of Chen et al.⁵¹ and Fang and Fu⁵² who employed 6-311+G(3df,2dp)^{39,55,56} and cc-pVDZ⁵⁷ basis sets, respectively. For example, the greatest absolute difference observed between the *R*_e(C-H), *R*_e(C-O), and *R*_e(O-O) values were 0.005, 0.020, and 0.025 Å, respectively. With respect to the *θ*_e(HCH) and *θ*_e(CO¹O²) bond angles, the absolute greatest discrepancies observed were 1.5 and 4.8°, respectively. The stable intermediate structure located on the triplet potential energy surface was also located using CCSD(T). This structure is consistent with that reported by Fang and Fu.⁵² Compared to the structure of (¹A')H₂C=OO, *R*_e(C-H), *R*_e(C-O), and *R*_e(O-O) for (³A'')H₂C=OO calculated using CCSD(T) were 1.163, 1.423, and 1.531 Å. The (³A'')H₂C=OO equilibrium bond angles calculated at this level of theory were 115.5 (*θ*_e(HCO¹)), 106.4 (*θ*_e(CO¹O²)), and -51.2° (*θ*_e(HCO¹O²)). In addition, the higher-spin triplet equilibrium structure lay 164.97 kcal mol⁻¹ above the (¹A')H₂C=OO species using CCSD(T)/6-311G**.

Equilibrium structures of the trans conformer of the methylperoxy radical calculated using B3LYP/6-31G** and CCS-

D(T)/6-311G** are given in Figure 3. This structure corresponds to a local minimum on the ²A'' [CH₃ + O₂] potential energy surface.⁴⁵ It was observed that these methods yielded equilibrium structures that were in good agreement. With respect to bond lengths, *R*_e(C-H), *R*_e(C-O), and *R*_e(O-O) calculated using these methods differed by 0.004, 0.003, and 0.005 Å, respectively. Similarly, the equilibrium bond angles *θ*_e(H¹CH³), *θ*_e(O¹CH¹), and *θ*_e(CO¹O²) differed by 1.8, 0.2, and 1.3°, respectively. This consistency was also evident in the calculated equilibrium *θ*_e(H²CO¹O²) dihedral angles, which differed by only 0.1°. Moreover, the *θ*_e(H¹CO¹O²) dihedral angle was identical using B3LYP/6-31G** and CCSD(T)/6-311G**. The cis form of the methylperoxy radical was also characterized here using CCSD(T)/6-311G**. This conformer (for which *θ*_e(H¹CO¹O²) = 0°) lay 1.19 kcal mol⁻¹ above the lower energy trans conformer. This is in good agreement with the B3LYP/6-311G(d,p) value of Zhu et al.,⁴⁵ being 0.8 kcal mol⁻¹. The cis conformer corresponds to a first-order transition state on the ²A''[CH₃ + O₂] potential energy surface. At the CCSD(T)/6-311G** level of theory, the imaginary frequency was 515.6 cm⁻¹, compared to the B3LYP/6-311G(d, p) value of 137 cm⁻¹.⁴⁵

Reaction Enthalpies. Enthalpies of reaction were determined here using ReaxFF, B3LYP/6-31G**, and the W1 composite method at 298.15 K. This facilitates comparison with experimental data, where available. Comparing Δ_rH°(298.15 K) data in this way will provide an indication as to the efficacy of both the predicted reaction mechanism and the overall simulation.

From Table 1, it is evident that for all reactions observed during the NVT-MD simulation, Δ_rH°(298.15 K) values calculated using ReaxFF are qualitatively consistent with experimental values and those calculated using both B3LYP/6-311G** and W1. Of all the reactions observed in the NVT-MD simulation, only four are endothermic. Moreover, it is evident that these endothermic processes were observed either during or soon after the initiation of the oxidative process. This is consistent with the total energy of the system shown in Figure 2a. For example, the reaction [CH₄ → C + 4H] exhibited a Δ_rH°(298.15 K) value of ca. 400 kcal mol⁻¹. The [CH₄ + O₂ → HO₂ + CH₃] and [H₂O₂ → 2OH] reactions both exhibited Δ_rH°(298.15 K) values of ca. 50 kcal mol⁻¹. The [CH₄ + H → H₂ + CH₃] reaction is also slightly endothermic, with Δ_rH°(298.15 K) being ca. 0.5 kcal mol⁻¹. With respect to the latter reaction, ReaxFF, B3LYP/6-311G**, and W1 gave consistent results with the experimental value of 0.6 ± 0.1 kcal mol⁻¹.⁵⁸

The hydrogenation of both C and CH are both exothermic processes. There was reasonable agreement between theoretical and experimental Δ_rH°(298.15 K) values for these reactions. For example, using ReaxFF, B3LYP/6-311G**, and W1, differences from experiment of ca. -37.3, 0.0, and 1.4 kcal mol⁻¹ were observed with respect to the hydrogenation of C. For the latter hydrogenation reaction these differences were, respectively, -13.5, -0.1, and 1.6 kcal mol⁻¹. The hydrogenation of O₂, HO₂, and OH were also observed to be exothermic. Moreover, there was better agreement between the methods employed here and experimental data. For example, for the reaction [O₂ + H → HO₂], ReaxFF, B3LYP/6-311G**, and W1 Δ_rH°(298.15 K) values were -69.8, -48.2, and -47.6 kcal mol⁻¹, and thus differed from experiment by -18.2, 3.4, and 4.0 kcal mol⁻¹. Similarly, for the [HO₂ + H → H₂O₂] reaction these differences were -13.6, 3.6, and -1.5 kcal mol⁻¹, whereas for the [OH + H → H₂O] reaction they were 5.0, 5.2, and 0.4 kcal mol⁻¹, respectively.

The addition of oxygen to the methyl and methylene radicals is an exothermic process. There is no experimental data concerning $[\text{CH}_2 + \text{O}_2 \rightarrow \text{H}_2\text{C}-\text{OO}]$ available in the literature. However, Chen et al.⁵¹ reported a $\Delta_r H^\circ(298.15 \text{ K})$ value for this addition reaction of $-49.1 \text{ kcal mol}^{-1}$ using CASPT2/6-311+G(3df,2p). Slagle and Gutman⁶⁰ reported a $\Delta_r H^\circ(298.15 \text{ K})$ of $-30.9 \pm 0.9 \text{ kcal mol}^{-1}$ for the $[\text{CH}_3 + \text{O}_2 \rightarrow \text{H}_3\text{C}-\text{OO}]$ reaction from experimental data. Zhu et al.⁴⁵ also reported a $\Delta_r H^\circ(298.15 \text{ K})$ value of $-30.4 \text{ kcal mol}^{-1}$ for this latter reaction using the G2 composite method.⁵⁹ The theoretical data listed in Table 1 regarding the addition of CH_3 and O_2 are in good agreement with experiment.⁶⁰ For example, B3LYP/6-311G** and W1 methods yield $\Delta_r H^\circ(298.15 \text{ K})$ values that were 1.2 kcal mol^{-1} greater and 0.3 kcal mol^{-1} smaller, respectively. This difference for the ReaxFF $\Delta_r H^\circ(298.15 \text{ K})$ value was larger, $-17.2 \text{ kcal mol}^{-1}$. Similar consistency was observed between these three theoretical methods for the formation of the Criegee intermediate. For example, $\Delta_r H^\circ(298.15 \text{ K})$ for the reaction $[\text{CH}_2 + \text{O}_2 \rightarrow \text{H}_2\text{C}-\text{OO}]$ calculated using ReaxFF was 11.6 and 14.6 kcal mol^{-1} larger than the B3LYP/6-311G** and W1 values, respectively. For the radical addition reaction $[\text{H}_3\text{C}-\text{OO} + \text{CH}_3 \rightarrow \text{H}_3\text{C}-\text{OO}-\text{CH}_3]$, these differences were -10.5 and $-6.2 \text{ kcal mol}^{-1}$, respectively.

Conclusions

Low-temperature POM was simulated using NVT-MD in conjunction with the ReaxFF hydrocarbon force field.²⁸ In particular, a $[20 \text{ CH}_4 + 10 \text{ O}_2]$ model system was simulated at 500°C . All reactions discussed were directly observed during the analysis of the computed trajectory of this model system. The mechanism observed during the NVT-MD simulation was subsequently analyzed using QM methods. In particular, B3LYP/6-311G** and CCSD(T)/6-311G** methods were employed to investigate the structures of several prominent species. Enthalpies of reaction were also computed using B3LYP/6-311G** and W1 methods. This comparison with QM and experimental data provided a good indication regarding the validity of the reaction mechanism observed during the NVT-MD simulation. The ReaxFF force field has therefore provided fundamental insight into the initial chemical mechanisms that feature during the partial oxidation of CH_4 .

The partial oxidative process was initiated by both the abstraction of hydrogen from CH_4 by O_2 and the atomization of CH_4 itself. Subsequent radical recombination of hydrogen was the primary mechanism by which H_2 was generated. However, the abstraction of hydrogen from CH_4 by hydrogen (i.e., forming CH_3 and H_2) was observed simultaneously. The final chemical composition of the system resulted from the sudden increase in the concentrations of radicals such as H , CH , CH_2 , CH_3 , OH , and HO_2 during the initiation of the oxidative process. Because of the high radical concentration during this period, radical recombination processes observed in the NVT-MD simulation resulted in species such as $\text{HC}=\text{O}$, HCO_2 , and $\text{H}_3\text{C}-\text{OO}-\text{CH}_3$. The methylperoxy and Criegee intermediate radicals were also observed during the NVT-MD simulation. The presence of these radicals was consistent with the conclusions of previous investigations of low-temperature combustion.^{45,48} Stoichiometric production of H_2 was not observed during the reaction; however, the percentage conversion of CH_4 was significantly larger than the value derived from recent experiments.¹²

Acknowledgment. A.J.P. thanks Dr. Adri van Duin of Pennsylvania State University for the use of the ReaxFF code

and his related advice and assistance. We acknowledge computing support from the Australian Centre for Advanced Computing and Communications (AC³) and the High-Performance Computing facility of the University of Newcastle, Australia.

References and Notes

- (1) Winter, J. C. *Int. J. Hydrogen Energy* **2004**, *29*, 1095.
- (2) Penner, S. S. *Energy* **2004**, *31*, 33.
- (3) Nowotny, J.; Sorrell, C. C.; Sheppard, L. R.; Bak, T. *Int. J. Hydrogen Energy* **2005**, *30*, 521.
- (4) Licht, S. *Chem. Commun.* **2005**, *37*, 4635.
- (5) Arakawa, H.; Aresta, M.; Armor, J. N.; Barteau, M. A.; Beckman, E. J.; Bell, A. T.; Bercaw, J. E.; Creutz, C.; Dinjus, E.; Dixon, D. A.; Domen, K.; DuBois, D. L.; Eckert, J.; Fujita, E.; Gibson, D. H.; Goddard, W. A.; Goodman, D. W.; Keller, J.; Kubas, G. J.; Kung, H. H.; Lyons, J. E.; Manzer, L. E.; Marks, T. J.; Morokuma, K.; Nicholas, K. M.; Periana, R.; Que, L.; Rostrup-Nielsen, J.; Sachtler, W. M. H.; Schmidt, L. D.; Sen, A.; Somorjai, G. A.; Stair, P. C.; Stults, B. R.; Tumas, W. *Chem. Rev.* **2001**, *101*, 953.
- (6) Das, D.; Veziroglu, T. N. *Int. J. Hydrogen Energy* **2001**, *26*, 13.
- (7) Irvine, J. J. *Mater. Chem.* **2008**, *18*, 2295.
- (8) York, A. P. E.; Xiao, T.; Green, M. L. H. *Top. Catal.* **2003**, *22*, 345.
- (9) Enger, B. C.; Lodeng, R.; Holmen, A. *Appl. Catal., A* **2008**, *346*, 1.
- (10) Wegang, R. S. *Fuel. Cell Bull.* **2001**, *28*, 8.
- (11) Moghtaderi, B.; Shames, I.; Djenidi, L. *Int. J. Heat Fluid Flow* **2006**, *27*, 1069.
- (12) Moghtaderi, B. *Fuel* **2007**, *86*, 469.
- (13) Pena, M. A.; Gomez, J. P.; Fierro, J. L. G. *Appl. Catal., A* **1996**, *144*, 7.
- (14) Tsang, S. C.; Claridge, J. B.; Green, M. L. H. *Catal. Today* **1995**, *23*, 3.
- (15) Zhu, Q.; Zhao, X.; Deng, Y. *J. Nat. Gas Chem.* **2004**, *13*, 191.
- (16) Liander, H. *Trans. Faraday Soc.* **1929**, *25*, 462.
- (17) Padovani, C.; Franchetti, P. G. *Chim. Ind. Appl. Catal.* **1933**, *15*, 429.
- (18) Prettre, M.; Eichner, C.; Perrin, M. *Trans. Faraday Soc.* **1946**, *42*, 335.
- (19) Brenner, D. W. *Phys. Rev. B* **1990**, *42*, 9458.
- (20) Tersoff, J. *Phys. Rev. B* **1988**, *37*, 6991.
- (21) Johnston, H. S.; Parr, C. J. *Am. Chem. Soc.* **1963**, *85*, 2544.
- (22) Johnston, H. S. *Adv. Chem. Phys.* **1960**, *3*, 131.
- (23) Root, D. M.; Landis, C. M.; Cleveland, T. J. *Am. Chem. Soc.* **1993**, *115*, 4201.
- (24) Cleveland, T.; Landis, C. M. *J. Am. Chem. Soc.* **1996**, *118*, 6020.
- (25) Landis, C. M.; Cleveland, T.; Firman, T. K. *J. Am. Chem. Soc.* **1998**, *120*, 2641.
- (26) Pauling, L. J. *J. Am. Chem. Soc.* **1947**, *69*, 542.
- (27) van Duin, A. C. T.; Dasgupta, S.; Lorant, F.; Goddard, W. A., III. *J. Phys. Chem. A* **2001**, *105*, 9396.
- (28) Chenoweth, K.; van Duin, A. C. T.; Goddard, W. A., III. *J. Phys. Chem. A* **2008**, *112*, 1040.
- (29) Strachan, A.; van Duin, A. C. T.; Chakraborty, D.; Dasgupta, S.; Goddard, W. A., III. *Phys. Rev. Lett.* **2003**, *91*, 098301.
- (30) Zhang, Q.; Cagin, T.; van Duin, A. C. T.; Goddard, W. A., III; Qi, Y.; Hector, L. G. *Phys. Rev. Lett.* **2004**, *69*, 045423.
- (31) van Duin, A. C. T.; Strachan, A.; Stewman, S.; Zhang, Q.; Xu, X.; Goddard, W. A., III. *J. Phys. Chem. A* **2003**, *17*, 3803.
- (32) Chenoweth, K.; Cheung, S.; van Duin, A. C. T.; Goddard, W. A., III; Kober, E. M. *J. Am. Chem. Soc.* **2005**, *127*, 7192.
- (33) Ludwig, J.; Vlachos, D. G.; van Duin, A. C. T.; Goddard, W. A., III. *J. Phys. Chem. B* **2006**, *110*, 4274.
- (34) Nielsen, K. D.; van Duin, A. C. T.; Oxgaard, J.; Deng, W.-Q.; Goddard, W. A., III. *J. Phys. Chem. A* **2005**, *109*, 493.
- (35) Goddard, W. A., III; Merinov, S. S.; van Duin, A. C. T.; Jacob, T.; Blanco, M.; Molinero, V.; Jang, S. S.; Jang, Y. H. *Mol. Simul.* **2006**, *32*, 251.
- (36) Berendsen, H. J. C.; Postma, J. P. M.; van Gunsteren, W. F.; DiNola, A.; Haak, J. R. *J. Phys. Chem. B* **1984**, *81*, 3684.
- (37) Becke, A. D. *J. Chem. Phys.* **1993**, *98*, 5648.
- (38) Lee, C.; Yang, W.; Parr, R. G. *Phys. Rev. B* **1998**, *37*, 785.
- (39) Krishnan, R.; Binkley, J. S.; Seeger, R.; Pople, J. A. *J. Chem. Phys.* **1980**, *72*, 650.
- (40) Merrick, J. P.; Moran, D.; Radom, L. *J. Phys. Chem. A* **2007**, *111*, 11683.
- (41) Martin, J. M. L.; de Oliveira, G. *J. Chem. Phys.* **1999**, *111*, 1843.
- (42) Frisch, M. J.; Trucks, G. W.; Schlegel, H. B.; Scuseria, G. E.; Robb, M. A.; Cheeseman, J. R.; Montgomery, J. A., Jr.; Vreven, T.; Kudin, K. N.; Burant, J. C.; Millam, J. M.; Iyengar, S. S.; Tomasi, J.; Barone, V.; Mennucci, B.; Cossi, M.; Scalmani, G.; Rega, N.; Petersson, G. A.; Nakatsuji, H.; Hada, M.; Ehara, M.; Toyota, K.; Fukuda, R.; Hasegawa, J.

- Ishida, M.; Nakajima, T.; Honda, Y.; Kitao, O.; Nakai, H.; Klene, M.; Li, X.; Knox, J. E.; Hratchian, H. P.; Cross, J. B.; Bakken, V.; Adamo, C.; Jaramillo, J.; Gomperts, R.; Stratmann, R. E.; Yazyev, O.; Austin, A. J.; Cammi, R.; Pomelli, C.; Ochterski, J. W.; Ayala, P. Y.; Morokuma, K.; Voth, G. A.; Salvador, P.; Dannenberg, J. J.; Zakrzewski, V. G.; Dapprich, S.; Daniels, A. D.; Strain, M. C.; Farkas, O.; Malick, D. K.; Rabuck, A. D.; Raghavachari, K.; Foresman, J. B.; Ortiz, J. V.; Cui, Q.; Baboul, A. G.; Clifford, S.; Cioslowski, J.; Stefanov, B. B.; Liu, G.; Liashenko, A.; Piskorz, P.; Komaromi, I.; Martin, R. L.; Fox, D. J.; Keith, T.; Al-Laham, M. A.; Peng, C. Y.; Nanayakkara, A.; Challacombe, M.; Gill, P. M. W.; Johnson, B.; Chen, W.; Wong, M. W.; Gonzalez, C.; Pople, J. A. Gaussian 03, revision E.01; Gaussian, Inc.: Wallingford, CT, 2004.
- (43) Stanton, J. F.; Gauss, J.; Watts, J. D.; Lauderdale, W. J.; Bartlett, R. J. *Int. J. Quant. Chem. Symp.* **1992**, 26, 879.
- (44) Srinivasan, N. K.; Micheal, J. V.; Harding, L. B.; Klippenstein, S. J. *Combust. Flame* **2007**, 149, 104.
- (45) Zhu, R.; Hsu, C.-C.; Lin, M. C. *J. Chem. Phys.* **2001**, 115, 195.
- (46) Petersen, E. L.; Davidson, D. F.; Hanson, R. K. *J. Propul. Power* **1999**, 15, 8291.
- (47) Petersen, E. L.; Kalitan, D. M.; Simmons, S.; Bourque, G.; Curran, H. J.; Simmie, J. M. *Proc. Combust. Inst.* **2007**, 31, 447454.
- (48) Simmie, J. M. *Prog. Energy Combust. Sci.* **2003**, 29, 599.
- (49) Taatjes, C. A.; Meloni, G.; Selby, T. M.; Trevitt, A. J.; Osborn, D. L.; Percival, C. J.; Shallcross, D. E. *J. Am. Chem. Soc.* **2008**, 130, 11883.
- (50) Andersen, A.; Carter, E. A. *J. Phys. Chem. A* **2003**, 107, 9463.
- (51) Chen, B.-Z.; Anglada, J. M.; Huang, M.-B.; Kong, F. *J. Phys. Chem. A* **2002**, 106, 1877.
- (52) Fang, D.-C.; Fu, X.-Y. *J. Phys. Chem. A* **2002**, 106, 2988.
- (53) Alvarez, R. A.; Moore, C. B. *J. Phys. Chem.* **1994**, 98, 174.
- (54) Huang, M.-B.; Chen, B.-Z.; Wang, Z.-X. *J. Phys. Chem. A* **2002**, 106, 5490.
- (55) Clark, T.; Chandrasekhar, J.; Spitznagel, G. W.; von Rague-Schleyer, P. *J. Comput. Chem.* **1983**, 4, 294.
- (56) Frisch, M. J.; Pople, J. A.; Binkley, J. S. *J. Chem. Phys.* **1984**, 80, 3265.
- (57) Woon, D. E.; Dunning, T. H. *J. Phys. Chem.* **1993**, 98, 1358.
- (58) Chase, M. W., Jr. *NIST-JANAF Thermochemical Tables*, 4th ed.; American Chemical Society: Washington, DC, 1998.
- (59) Curtiss, L. A.; Raghavachari, K.; Trucks, G. W.; Pople, J. A. *J. Chem. Phys.* **1991**, 94, 7221.
- (60) Slagle, I. R.; Gutman, D. *J. Am. Chem. Soc.* **1985**, 107, 5432.

JP809576K